Tenth International Conference on Computational Fluid Dynamics (ICCFD10), Barcelona, Spain, July 9-13, 2018

ICCFD10-102

Numerical Simulation of Dynamic Stall Using Near-Body Adaptive Mesh Refinement

Neal M. Chaderjian*

*NASA Ames Research Center, Moffett Field, CA, 94035, USA

Abstract: Time-dependent Reynolds-averaged Navier-Stokes simulations have been carried out for a NACA 0012 airfoil and a flexible UH-60A rotor undergoing dynamic stall. The OVERFLOW computational fluid dynamics (CFD) code is used to explore the use of near-body adaptive mesh refinement (NB-AMR) for the first time on a flexible helicopter rotor in forward flight. Emphasis is placed on understanding the temporal and spatial convergence of the solutions, their numerical efficiency and stability, and establishing a grid-converged solution. Some of the remaining differences between CFD and flight-test measurements are discussed. Time-dependent flow visualization is used to provide an improved understanding of the physical mechanisms involved with two-dimensional and three-dimensional dynamic stall, and the NB-AMR process.

1. Introduction

Helicopters perform many useful civil and military functions by virtue of their ability to take off and land vertically without a runway or hover in place. Some examples include military or remote location deployment, medical or emergency evacuation, combating forest fires, police surveillance, and heavy-lift construction. However, helicopter aerodynamics is often more complex than a fixed-wing aircraft because the main rotor is very flexible and must perform several functions, e.g., generate the necessary forces and moments needed to keep the vehicle aloft, provide a propulsive force for forward flight and balance all moments needed for trimmed level flight. Rotorcraft flow simulation is therefore inherently time-dependent and multi-disciplinary, combining computational fluid dynamics (CFD), computational structural dynamics (CSD), and a trim algorithm to establish the blade-root motions for level flight.

A condition known as blade vortex interaction (BVI) may also occur when the tip vortex of one blade interacts with the other rotor blades, producing unsteady airloads, noise and vibrations. Moreover, dynamic stall is a dangerous condition that occurs when a rotor reaches its thrust limit due to blade stall. This condition often produces large blade torsion and control system loads and limits the flight speed of the helicopter [1]. The time-dependent Reynolds-averaged Navier-Stokes (RANS) equations are solved using the OVERFLOW [2-3] CFD code for an isolated, flexible UH-60A rotor in forward flight, see Figs. 1-2. The flight condition examined in this paper involves both BVI and dynamic stall.

Chaderjian et .al [4-5] showed that hover performance and blade loading was not a strong function of resolving the blade-tip vortices in the rotor wake, as it was previously thought. Rather, it was more important to resolve the vortex formation at the blade tip using a combination of fine surface meshes and high-order spatial accuracy, at least 5^{th}-order spatial accuracy, and maintaining a physically realistic turbulent eddy viscosity in the rotor wake using a detached eddy simulation (DES) turbulent length scale. Moreover, Chaderjian [6] recently showed that rotor performance for the UH-60A rotor in forward flight also did not depend significantly on resolving the tip vortices in the rotor wake, even for more challenging BVI and dynamic stall cases. So, engineering resolution of the rotor wake is sufficient for predicting

rotor airloads, i.e., $\Delta S = 10\%\ c_{tip}$, where ΔS is the Cartesian grid spacing in the rotor wake and c_{tip} is the blade-tip chord length. In these studies, OVERFLOW's off-body adaptive mesh refinement (OB-AMR) was used to resolve the rotor wake using $\Delta S = 10\%$, 5%, and 2.5% c_{tip}. However, Lim et al. [7] and Jia et al. [8] showed that $\Delta S = 5\%\ c_{tip}$ is needed for accurate acoustic prediction in strong BVI cases. Using $\Delta S = 10\%\ c_{tip}$ can result in an underprediction of acoustic levels by 5dB, a significant difference.

Figure 1 Sikorsky UH-60A Blackhawk helicopter on apron. Note flexible blades.

Figure 2 Sikorsky UH-60A Blackhawk helicopter in flight.

Although the prediction of dynamic stall for the UH-60A rotor (flight counter C9017) is generally good [6], there are some deficiencies in the predicted normal force and pitching moment coefficients, C_n and C_m, respectively. This occurs surprisingly along the outer blade stations near azimuth angles of $\psi = 90°$ and 180° (see Fig. 16) where the flow is attached but experiencing BVI. On the other hand, C_n and C_m are better captured in the dynamic stall region where $225° \le \psi \le 360$. An important question remains: What is the cause of this discrepancy? It seems unlikely that the turbulence model is the primary source for these differences since the forces and moments are well captured in the dynamic stall region. Other potential causes are inadequate grid resolution on the rotor blades, uncertainty in the aeroelastic blade properties, or possibly the flight-test measurements themselves. For example, anomalous behavior of certain pressure taps is occasionally apparent on the advancing side, but not the retreating side [9].

The goal of this paper is to examine the effects of rotor-blade grid refinement on the predicted rotor airloads for dynamic stall flight counter C9017. This is the first time OVERFLOW's near-body adaptive mesh refinement (NB-AMR) is used on a flexible rotor blade in forward flight. Establishing a grid-resolved solution will help eliminate one potential cause for the discrepancies of the predicted forces and moments. Convergence, stability and efficiency of the numerical approach will also be examined and time-dependent flow visualization will be used to better understand the fluid physics of dynamic stall.

The following sections include a discussion of the flight-test data, numerical approach, results and discussion, and concluding remarks.

2. Flight-Test Data

NASA and the US Army, as a part of the UH-60A Airloads program, maintain an extensive flight-test database [10] for the Blackhawk helicopter (Figs. 1-2) in level trimmed flight and executing transient maneuvers. The UH-60A blade properties are listed in Table 1, while Table 2 lists two flight conditions discussed in this paper. The dynamic stall case, flight counter C9017, is the primary subject of this paper. The advance ratio, μ, is a key parameter in forward flight and is the ratio of the freestream speed (V_∞) to the blade-tip speed (V_{Tip}), or equivalently freestream Mach number (M_∞) and blade-tip Mach number (M_{Tip}), respectively. The blade-tip Reynolds number (Re_{Tip}), rotor shaft angle (α_s), sideslip angle (β), and thrust coefficient (C_T) are also given in Table 2.

Table 1 UH-60A rotor parameters.

Parameter	Value
Number of Blades	4
Radius, R	26.83 ft
Tip Chord, c_{tip}	20.76 in
Equivalent Blade Twist	-18 deg
Blade Tip Sweep	20 deg aft
Geometric Solidity, σ	0.0826
Airfoils	SC1095/SC1094R8
Thickness	9.5% chord
Nominal Rotor Speed	258 rpm
Nominal Tip Speed	725 ft/sec

Table 2 Selected flight counter flow conditions.

Flight Counter	M_∞	M_{Tip}	μ	Re_{Tip}	α_s, deg	β, deg	C_T
C8534 (High Speed)	0.236	0.642	0.368	6.86×10^6	-7.31	1.28	0.00651
C9017 (Dynamic Stall)*	0.158	0.666	0.237	4.62×10^6	-0.15	-1.58	0.0110

* Flow condition studied in this paper.

The UH-60A airloads database provides aerodynamic pressures, structural loads, control positions, and rotor forces and moments at 9 radial locations shown in Fig. 3. A static trim tab is deflected to ensure that each blade flies in a similar manner with minimal vibration. These deflections are unique to each Blackhawk helicopter, and the CFD simulations assume zero deflection.

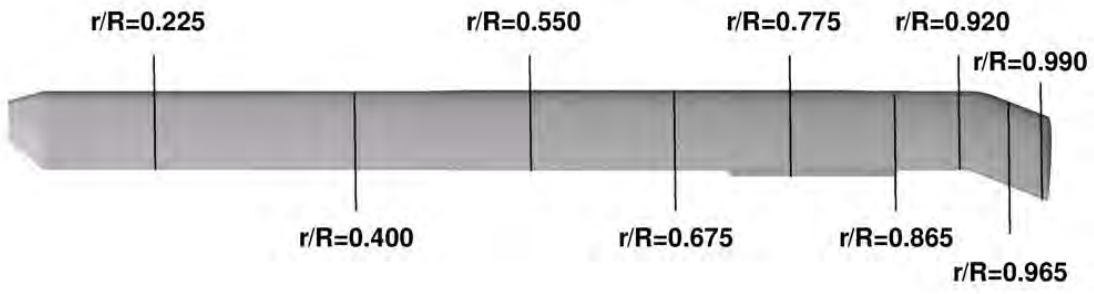

Figure 3 UH-60A flight-test measurement stations [10].

Acquiring in-flight measurements on a moving and deforming rotor blade is very challenging, and this database does have some unresolved discrepancies. For example, the measured rotor thrust was determined from the helicopter's gross weight and estimates of the loads on the fuselage and tail rotor. Measured pitch and roll moments at the hub were determined from a bending moment gauge located on the upper rotor shaft. But an integration of the measured blade pressures sometimes compared poorly with the measured thrust and moments. For example, Potsdam et al. [11] point out that the integrated thrust for flight counter C8534 was 10% higher than the measured thrust. Moreover, the integrated hub moment was 50% larger with an 80-deg phase difference compared to the measured pitching moment. Some of these discrepancies have been attributed to the discovery of bad pressure taps, with the greatest effect on the pitching moments. It is therefore common practice to subtract out the mean forces and

moments over a rotor revolution for validating CFD results with this flight-test data. That is the practice adopted in this paper.

3. Numerical Approach

The OVERFLOW CFD code is used to solve the time-dependent Reynolds-averaged Navier-Stokes equations for an isolated UH-60A rotor in forward flight. This CFD code has a variety of implicit and relaxation algorithms that utilize upwind and central spatial differencing. Both single and dual time integration options are available. Curvilinear and Cartesian overset grids are used to treat complex geometries and the surrounding flow domain. A variety of zero, one, and two-equation turbulence models are available to solve the RANS equations. For more complex flows, transition trip lines and models, and detached eddy simulation (DES) are useful options. A more complete description of the OVERFLOW CFD code and its user's manual can be found in Refs. [2-3]. Some of the key aspects used in the present computations are described below.

3.1 Overset Grids

The current time-accurate approach consists of an inertial coordinate system where overset body-conforming O-grids rotate through a fixed Cartesian background grid system. Figure 4a-b shows the near-body (NB) grids that are used to resolve the flow in the vicinity of the rotor blades. Each rotor blade consists of 4 grids: one inboard cap grid, two main body grids, and one outboard cap grid. The two cap grids resolve the inboard blade root and outboard blade tip. The main blade O-grid is split into upper and lower grids since the NB-AMR algorithm does not allow for periodic grids. Three NB grids are also used to resolve the flow on a simplified rotor hub, see Fig. 4c. The hub rotates with the rotor blades, however, the linkages between the hub and the blades are very complex and neglected.

Surface grid resolution on the rotor blades is clustered in the chordwise direction near the airfoil leading and trailing edges to accurately resolve high pressure gradients. The spanwise resolution along the rotor blade is nearly uniform, but clustered near the blade tip to accurately resolve the formation of the tip vortices. The viscous grid spacing near the rotor-blade surface ensures that $y^+ < 1$ over most of the blade. These fine blade grids represent a best attempt to resolve the flow without NB-AMR. All curvilinear body grids have a stretching ratio of less than 10% in all three coordinate directions. This reduces the algorithm truncation error associated with 2^{nd}-order accurate grid transformation metrics.

An off-body (OB) Cartesian grid system, also shown in Fig. 4c, is designed to resolve the off-body vortex wake and extend the computational domain to the far field. The grid transformation metrics are constant due to uniform Cartesian grid spacing. Solutions are obtained by using a uniform Cartesian grid spacing of $\Delta = 5\% c_{tip}$ on the first set of Level one (L_1) grids that completely surround the rotor. Additional "brick grids" are automatically added to the L_1 grids to rapidly extend the computational domain to the far field, which for the present computations is 5 rotor radii (R) from the blades. These brick grids are referred to as Levels 2, 3, …, each of which is a factor of 2 coarser in every direction than the previous grid level. Table 3 summarizes grid size statistics for the baseline NB grids before any AMR.

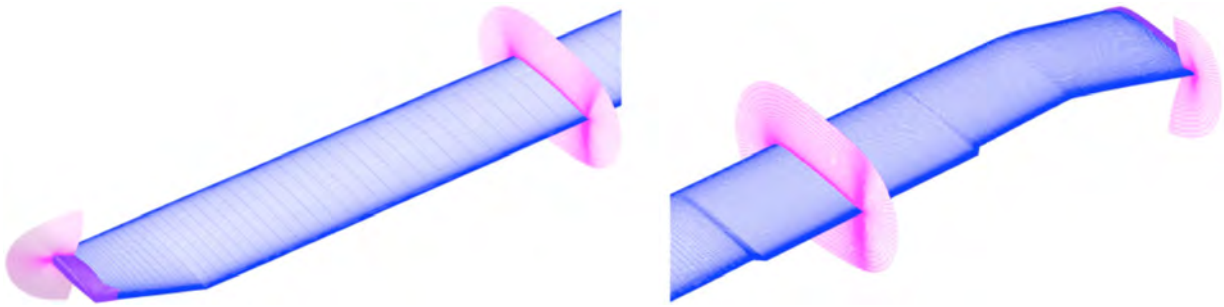

a) Inboard NB rotor blade grids. b) Outboard NB rotor blade grids.

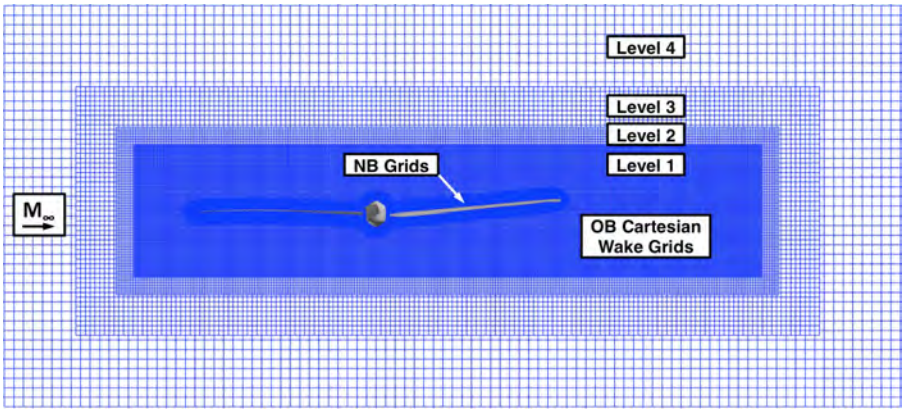

c) Cartesian OB grid system.

Figure 4 UH-60A rotor-blade overset grid system.

Table 3 Summary of UH-60A baseline overset grid size.

Grid Type	Number of Grids	Surface Grid Points	Volume Grid Points
Rotor Blade	4	117,763	11.8 million
Rotor Hub	3	28,875	2.5 million
4-Bladed Rotor with Hub	19	499,927	49.7 million

3.2 Numerical Algorithm

The Navier-Stokes equations in strong conservation-law form are given by

$$\frac{\partial Q}{\partial t} + \frac{\partial (F - F_v)}{\partial x} + \frac{\partial (G - G_v)}{\partial y} + \frac{\partial (H - H_v)}{\partial z} = 0 \tag{1}$$

where $Q=[\rho,\ \rho u,\ \rho v,\ \rho w,\ e]^T$ is the vector of conserved variables, i.e., density, momentum and total energy; F, G, and H are the inviscid flux vectors; and F_v, G_v, and H_v are the viscous flux vectors. An implicit approximate factorization scheme in delta form is used to solve Eq. (1) in generalized curvilinear coordinates, and is given by

$$\left[I + h\partial_\xi \hat{A}^k\right]\left[I + h\partial_\eta \hat{B}^k\right]\left[I + h\partial_\zeta \hat{C}^k\right]\Delta\hat{Q}^k = -hR^{k,n} \tag{2}$$

Where

$$R^{k,n} = \frac{3\hat{Q}^k - 4\hat{Q}^n + \hat{Q}^{n-1}}{2\Delta t} + (\hat{F} - \hat{F}_v)^k_\xi + (\hat{G} - \hat{G}_v)^k_\eta + (\hat{H} - \hat{H}_v)^k_\zeta$$

and

$$h = \frac{2\Delta t \Delta \tau}{2\Delta t + 3\Delta \tau}$$

In these equations, $\hat{Q} = Q/J$, where J is the coordinate transformation Jacobian. The superscript k is the sub-iteration index, while the superscript n is the time-step index. The physical and pseudo (relaxation) time steps are Δt and $\Delta \tau$, respectively. Finally, $\Delta \hat{Q}^k = \hat{Q}^{k+1} - \hat{Q}^k$, where sub-iteration convergence implies that $\hat{Q}^k \to \hat{Q}^{n+1}$, which is 2nd-order accurate in time.

Equation 2 is solved using the Pulliam-Chaussee [12] diagonal algorithm. A baseline time step of Δt=¼° rotation with 100 sub-iterations is used. This nominally exceeds a 2.5-order L_2-norm sub-iteration drop between time steps. The application of NB-AMR may require smaller time steps to maintain a reasonable number of sub-iterations. Throughout this sub-iteration process the Navier-Stokes algorithm becomes fully implicit and the approximate factorization and time linearization errors are sufficiently removed.

Central differencing is used for all spatial operators throughout this paper. For example, the convective terms use 6th-order central differences with a 5th-order artificial dissipation term to damp out high-frequency errors. This results in a 5th-order accurate discretization on the uniform Cartesian OB grids. However, all viscous terms are evaluated with 2nd-order accurate central differences. The grid metrics on the curvilinear NB grids are also 2nd-order accurate in space. This discretization is referred to as 5th-order spatial differencing throughout this paper. Although the algorithm is still formally 2nd-order accurate in space, computed results show that this differencing scheme has lower diffusion and dispersion errors, and an improved flow field resolution than a 3rd-order approach. Table 4 summarizes the convective central difference operators available in OVERFLOW. Further details are described by Pulliam [13].

Table 4 Convective central difference operators.

Cartesian Wake Grid Accuracy	Difference Stencil	Artificial Dissipation
$O(\Delta X^2)$	$\delta_X^{(2)}$	$\sim(\Delta X^3)\delta_{X^4}$
$O(\Delta X^3)$	$\delta_X^{(4)}$	$\sim(\Delta X^3)\delta_{X^4}$
$O(\Delta X^4)$	$\delta_X^{(4)}$	$\sim(\Delta X^5)\delta_{X^6}$
$O(\Delta X^5)$	$\delta_X^{(6)}$	$\sim(\Delta X^5)\delta_{X^6}$
$O(\Delta X^6)$	$\delta_X^{(6)}$	$\sim(\Delta X^7)\delta_{X^8}$

3.3 Adaptive Mesh Refinement

An AMR capability is available in OVERFLOW to dynamically resolve flow features with finer meshes within the off-body Cartesian grids, Fig. 4c, and within the curvilinear near-body grids, Fig. 4a-b. A brief description of the procedure is now provided.

OB-AMR begins with a baseline Cartesian Level-1 grid that surrounds the rotor with resolution ΔS. The rotor wake can be further refined with AMR through successively finer overlapping grids. Each level of refinement decreases the local Cartesian grid spacing by a factor of one half in each coordinate direction, i.e., the refinement is isotropic in space. Thus, a two-level OB-AMR refinement would identify the vortex-wake structures and overlay the surrounding Level-1 Cartesian grid spacing (ΔS) with two more Cartesian grids with grid spacing ½ ΔS and ¼ ΔS. An example for a rotor in hover is shown in Fig. 5. The local grid size grows by 8X for

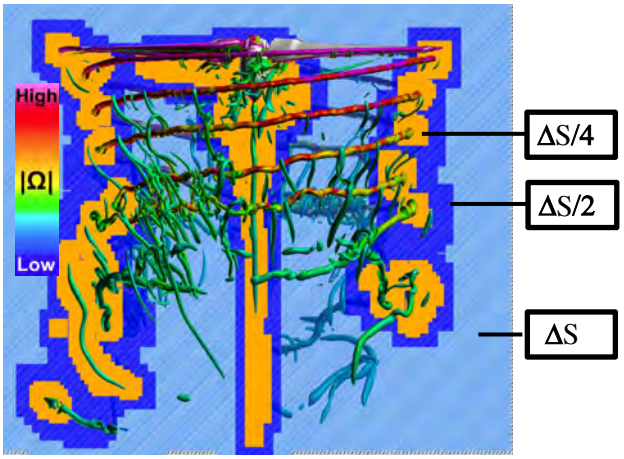

Figure 5 Example of OVERFLOW two-level dynamic AMR grid system for a rotor in hover [4-5]. Vortices colored by vorticity magnitude, OB-AMR grid spacing ΔS=10% ctip, ΔS/2, ΔS/4.

each level of refinement. This approach is more efficient than selecting a single larger Cartesian region of grid spacing ¼ ΔS to resolve the entire rotor wake. Overlapping grids of different resolution transfer data between grids with tri-linear interpolation. The AMR process can be limited so that only regions of interest are refined rather than continuing indefinitely throughout the entire flow field.

A somewhat different OB-AMR strategy is employed in this paper that eliminates interpolation errors within the resolved rotor wake for dynamic stall case C9017. This is accomplished by only using Level-1 grids to automatically capture and resolve the rotor wake region (see Fig. 6). Level-1 grids share the same grid spacing, ΔS, and therefore have coincident grid points when they overlap with each other. Data is therefore transferred between these Level-1 wake grids by direct injection, i.e., no interpolation is required. Tri-linear interpolation is only needed when dissimilar grids overlap with each other.

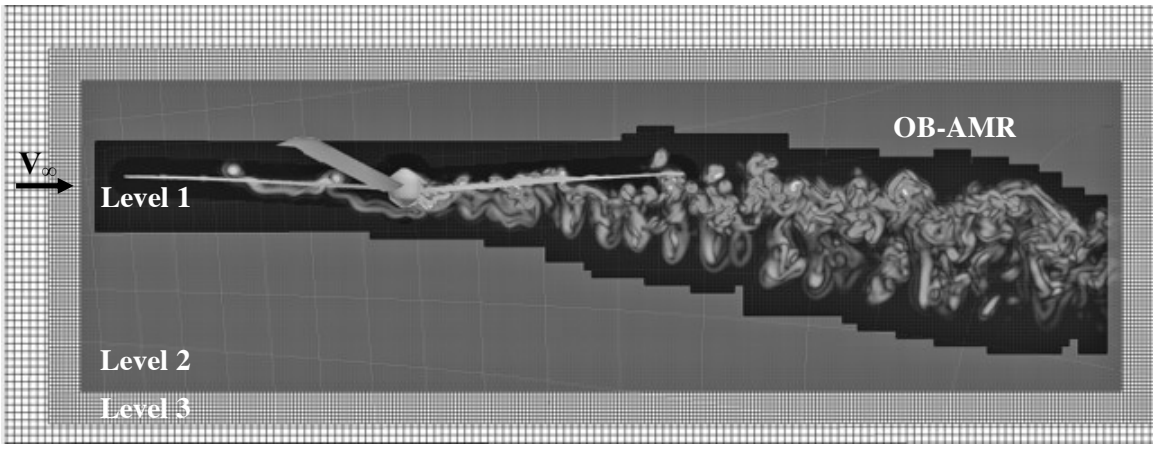

Figure 6. Side view of vortex wake resolved with OB-AMR Level-1 grids (vorticity magnitude gray scale). Flight counter C9017, ΔS=5% c_{tip}, 3700 grids, 210 million grid points.

The AMR process depends on a sensor function, *SF*, and user-specified parameters that determine where to refine, coarsen, or leave the grid resolution unchanged. References [4-6] used a vorticity magnitude sensor function for OB-AMR. With this approach, once a threshold is reached, grid refinement is carried out to the fullest amount specified. So, a two-level refinement will refine the local mesh to ΔS/4, or a three-level refinement to ΔS/8, etc.

Another approach, and the one used in this paper, uses a 2nd-order undivided difference. The term "undivided" refers to the difference not being divided by the appropriate grid cell size term, i.e., Δx for the first-difference, Δx^2 for the second difference, etc. In the context of computing *SF* as a general sensor function for adaption, it is (a) normalize by a reference quantity Q_{ref}, (b) square it to create a non-negative value, (c) take the maximum over all elements of Q, and (d) take the maximum over all coordinate directions:

$$SF = \max_{i=j,k,l} \left\{ \max_{Q \text{ components}} \left[\left(\frac{Q_{i-1} - 2Q_i + Q_{i+1}}{2\,Q_{ref}} \right)^2 \right] \right\} \tag{3}$$

This function is non-dimensional, independent of grid units, and becomes smaller as the grid is refined (where Q is smooth), all desirable properties for a sensor function for solution adaption. Further, it is simple to compute and the computation can be fully parallelized. Equation 3 therefore refines the local mesh in regions of high solution curvature. The AMR process is carried out in such a manner so that all adjacent overlapping grids differ by no more than 2x the grid spacing, see Fig. 11. Further details of the OB-AMR process are described by Buning and Pulliam [14].

The NB-AMR is carried out is a similar manner as the OB-AMR. However, the NB-AMR operates on curvilinear grids, which look Cartesian in computational (or index) space. Parametric cubic interpolation is used to transfer data between grids of different resolution. This approach preserves smooth geometry, avoiding faceting of the surface that would occur with linear interpolation. Further details of the NB-AMR process are described by Buning and Pulliam [15].

3.4 Turbulence Model

The rotor simulations presented in this study use the one-equation Spalart-Allmaras (SA) turbulence model [16]. Some of the model's key features are now described.

The SA model uses the Boussinesq approximation to relate the Reynolds stresses to a kinematic turbulent eddy viscosity and the mean strain-rate tensor. The turbulent eddy viscosity (TEV) is given by

$$\nu_t = \tilde{\nu} f_{v1}$$

The SA transport equation for the variable $\tilde{\nu}$, is given by

$$\frac{D\tilde{\nu}}{Dt} = \underbrace{C_{b1}\tilde{\nu}\left(\Omega + \frac{\tilde{\nu}}{k^2 d^2} f_{v2}\right)}_{\text{Production}} - \underbrace{C_{w1} f_w \left(\frac{\tilde{\nu}}{d}\right)^2}_{\text{Dissipation}} + \underbrace{\frac{1}{\sigma}\left[\nabla \cdot \left((\nu + \tilde{\nu})\nabla\tilde{\nu}\right) + C_{b2}(\nabla\tilde{\nu})^2\right]}_{\text{Diffusion}} \tag{4}$$

where D/Dt is the material time derivative. The right hand side consists of production, dissipation and diffusion source terms. The constants C_{b1}, C_{b2}, C_{w1}, k, σ, and functions f_{v1}, f_{v2}, f_w, are described by Spalart and Allmaras [16], and Ω is the magnitude of vorticity. The damping function, f_{v1}, reduces ν_t near a solid wall, i.e., the laminar sublayer. The turbulent length scale, d, is defined as the distance to the nearest wall.

Rotor blade-tip vortices are a dominant structure in the turbulent rotor wake. They are initially formed at the rotor tip by the roll-up of the blade trailing edge shear layers. Figure 7 is a laser light sheet flow visualization of a fully formed tip vortex reported by Ramasamy et al. [17]. He identified three vortical regions. The outer region 3 can be characterized by a turbulent flow whose mean velocity field is similar to a potential vortex. Region 2 is an intermediate state that contains turbulent eddies of varying size. The inner-most region 1 can be characterized as stratified layers having few or small eddies with little interaction between fluid layers, due to high streamwise curvature. This inner-core region has a near-linear velocity profile and very low fluid strain.

Regions of high streamline curvature reduce the fluctuating velocity components and hence the turbulent production. Shur et al. [18] introduced a SA rotation and/or streamline curvature (SARC) correction for rotating and curved flows. The SARC correction not only improves the boundary layer profiles for highly curved flows, but also helps reduce the TEV in the tip vortex cores. The SARC correction is used for all SA turbulent simulations in this paper.

An additional degree of realism can be obtained by the use of large eddy simulation (LES). In LES the largest turbulent eddies are resolved using a small grid spacing, Δ, and the subgrid-scale (SGS) eddies are modeled. Smagorinsky [19] first postulated a SGS model for the Reynold's stresses based on the following expressions

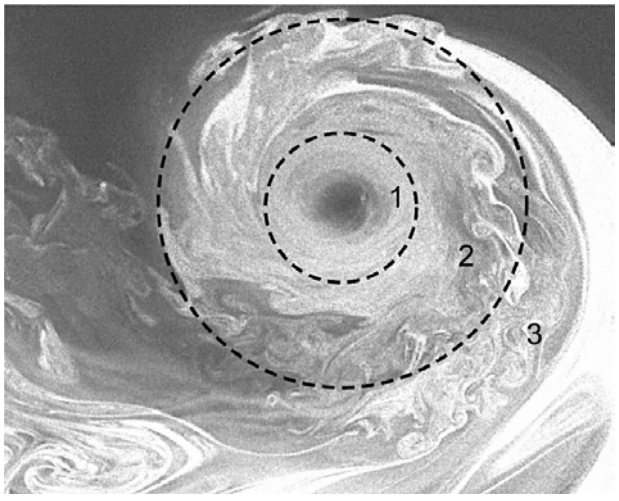

Figure 7 Laser light sheet flow visualization of a fully developed blade-tip vortex, Ramasamy et al. [17].

$$\tau_{ij} = 2\nu_t S_{ij},\ S_{ij} = \frac{1}{2}\left(\frac{\partial u_i}{\partial x_j} + \frac{\partial u}{\partial x_i}\right) \tag{5}$$

where S_{ij} is the strain-rate tensor, ν_t is the Smagorinsky eddy viscosity given by

$$\nu_t = \left(C_s\Delta\right)^2\sqrt{S_{ij}S_{ij}} \tag{6}$$

and C_s is the Smagorinsky coefficient. In this expression, $\Delta=(\Delta x\cdot\Delta y\cdot\Delta z)^{1/3}$, i.e., the geometric mean of the grid cell spacing. Use of LES to wall resolve the turbulent boundary layers on the rotor blades and hub could easily result in trillions of grid points. This is beyond the scope of modern supercomputers for rotor flow fields at flight Reynolds numbers. However, Spalart et al. [20] suggested detached eddy simulation (DES) as a more practical alternative.

DES can be viewed as a blending of the SA-RANS turbulence model in boundary layers with coarse-mesh LES in regions of separated flow, or where the largest eddies are to be grid resolved. This hybrid RANS/LES approach is accomplished by replacing the distance to the nearest surface (d) by

$$\tilde{d} = \min\left(d, C_{DES}\Delta\right) \tag{7}$$

where $\Delta=\max(\Delta x, \Delta y, \Delta z)$, and $C_{DES}=0.65$. In this way the SA-RANS model becomes the SGS model. Moreover, it is easy to show that when production balances dissipation in Eq. 4, and when $\tilde{d}$ is used as the length scale, then ν_t simplifies to a Smagorinsky-type model. So, the SA-DES model behaves like an LES-type model when the grid support is sufficiently small.

The SA-DES approach can be viewed in two ways. From a numerical point of view, it reduces the TEV in the rotor wake to more realistic values. This is an important result as it has been shown [4-5] that a RANS length scale can result in very large TEV in the case of a hovering rotor. This non-physical TEV can work its way up the vortex wake and infiltrate the rotor blade boundary layers, causing a rapid increase in blade drag and rotor torque. The result is an artificially low prediction of hover performance. From a physical point of view, the SA-DES approach can be viewed as resolving the largest turbulent eddies outside the boundary layer. This results in a more realistic numerical simulation of the turbulent hover performance.

This simple and elegant approach effectively reduces the TEV to more realistic values outside the boundary layer. However, as the mesh is refined, e.g., with NB-AMR, LES mode may be prematurely activated, causing a stress depletion and non-physical flow separation. Spalart et al. [21] introduced a correction called delayed detached eddy simulation (DDES). This shielding function prevents the inadvertent use of LES mode too close to the rotor blade surface. This hybrid RANS/LES model is used for three-dimensional flows in this paper and referred to as SA-DDES.

3.5 Blade Motions

The helicopter rotor blades undergo a periodic motion applied where the hub is linked to the rotor blades. Three angles, θ, β, and ζ are defined as the pitch, flap, and lag angles, respectively. The pilot commands the pitch angle while the flap and lag angles are reactions at the hub/blade linkage. These angles are supplied to the CFD simulation by the trim algorithm, and defined by a Fourier series

$$\begin{pmatrix}\theta\\ \beta\\ \zeta\end{pmatrix} = \begin{pmatrix}\theta_\circ + \theta_{1c}\cos\psi + \theta_{1s}\sin\psi + \cdots\\ \beta_\circ + \beta_{1c}\cos\psi + \beta_{1s}\sin\psi + \cdots\\ \zeta_\circ + \zeta_{1c}\cos\psi + \zeta_{1s}\sin\psi + \cdots\end{pmatrix} \tag{8}$$

Normally the series is truncated after the first harmonic unless there is a need for higher harmonic blade control. The collective, $\theta_\circ$, is the mean pitch angle that controls the thrust. The θ_{1c} and θ_{1s} angles are the lateral cyclic and longitudinal cyclic, with a period of one/revolution. They control the rotor tip path plane, i.e., the tilt of the thrust vector. Similar definitions apply to the flap angle, $\beta_\circ$, and lag angle, $\varsigma_\circ$. The actual motion of a point on a rotor blade surface is the sum of the supplied motions at the blade root, Eq. 8, plus any aeroelastic deformations.

3.6 CFD/CSD Loose Coupling

The UH-60A rotor blade is very flexible and responds to CFD airloads and blade motions. Moreover, the time-varying blade angles supplied at the blade root must be iteratively determined to obtain the required thrust and hub moments for trimmed level flight. The CFD and CSD interaction is modeled by loosely coupling (LC) the OVERFLOW CFD code with the helicopter comprehensive analysis code, CAMRAD II [22]. As the name implies, helicopter comprehensive analysis codes provide a comprehensive engineering analysis for rotorcraft design, e.g., aerodynamics, structures, flight trim algorithm, flutter analysis, aeroacoustic analysis, etc.

CAMRAD II is widely used in the helicopter industry and models a flexible rotor blade using nonlinear finite elements. It has its own simplified aerodynamic model that uses blade element theory, two-dimensional airfoil tables, and vortex wake models. A complete helicopter solution for trimmed flight can be obtained in less than one minute using a single CPU.

High fidelity time-periodic solutions for the UH-60A rotor system are obtained by loosely coupling OVERFLOW with CAMRAD II (see Fig. 8). This coupling is done in a time-periodic manner, as specified by the user. The coupling period is some fraction of the number of rotor blades. In the case of the four-bladed UH-60A rotor, coupling periods of ¼, ½, and 1 revolution are typical. The lower coupling periods often provide faster LC convergence, provided the process is stable. A coupling period of ¼ revolution is used in this study.

A LC iteration involves OVERFLOW providing CAMRAD II with Navier-Stokes rotor blade loads. Then CAMRAD II provides OVERFLOW with a new set of blade deformations and blade angles applied at the blade root. If the forces, moments and supplied angles are converged to the trim flight condition, then the LC is complete, otherwise another LC iteration is performed.

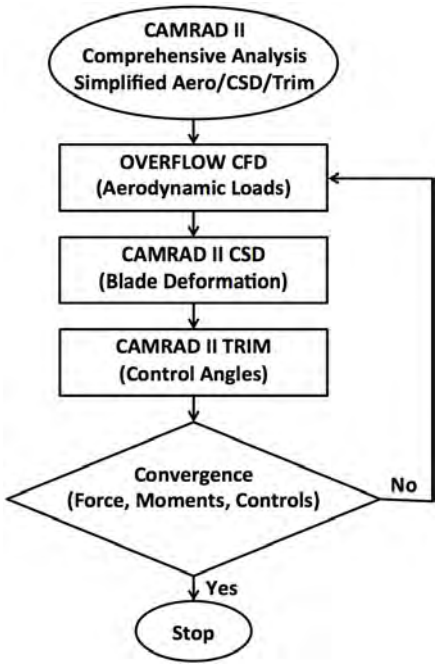

Figure 8 Loose coupling process for CFD/CSD/trim.

OVERFLOW airloads are transferred to CAMRAD II according to the expression

$$\begin{aligned}(F,M)_{Total}^{l_c+1} &= (F,M)_{CAero}^{l_c} + \left((F,M)_{CFD}^{l_c} - (F,M)_{CAero}^{l_c-1}\right) \\ &= (F,M)_{CFD}^{l_c} + \left((F,M)_{CAero}^{l_c} - (F,M)_{CAero}^{l_c-1}\right)\end{aligned} \tag{9}$$

where (F,M) corresponds to rotor blade sectional forces and moments at the 1/4-chord location. Superscript l_c is the LC step, subscript "*CAero*" refers to CAMRAD II aerodynamics model, and subscript "*Total*" refers to the total airloads applied to the deforming rotor blades within the CAMRAD II code. Note that as the LC process converges,

$$(F,M)_{Total} = \lim_{l_c\to\infty} (F,M)_{CFD}^{l_c} + \left((F,M)_{CAero}^{l_c} - (F,M)_{CAero}^{l_c-1}\right) = (F,M)_{CFD} \tag{10}$$

In other words, in the limit the total airloads applied to the flexible rotor blades within CAMRAD II are the OVERFLOW Navier-Stokes airloads. This process tends to converge rapidly, often within 5 rotor revolutions from impulsive start using ¼-rev LC steps.

The CAMRAD II trim algorithm provides the blade root angles for steady trimmed flight by solving a nonlinear system of equations using the Newton-Raphson method. These equations describe the total force and moment response for the entire rotorcraft to perturbations in the control angles. CAMRAD II

supplies the aerodynamic loads due to the other vehicle components. Potsdam et al. [11] provide a detailed description of the delta airloads loose coupling process.

Finally, the assumption of time-periodic airloads on the rotor blades is a fundamental assumption to the time-accurate LC process. There may be some aperiodicity in the rotor wake, which is often the case, but the rotor blade airloads are required to be sufficiently periodic. The LC process is therefore unable to simulate non-periodic vehicle maneuvers.

4. Results and Discussion

The OVERFLOW Navier-Stokes CFD code is used throughout this study for a NACA 0012 airfoil oscillating in angle of attack and an isolated UH-60A rotor in forward flight. Both cases involve dynamic stall and use 2nd-order dual-time accuracy and 5th-order central differences with added artificial dissipation. The SA-RANS turbulence model is used for the 2D airfoil problem while the SA-DDES turbulence model is used for the 3D UH-60A rotor. The SARC rotational correction is used for both cases.

All CFD results have been carried out on the NASA Advanced Supercomputing (NAS) facility at Ames Research Center using the Pleiades and Electra supercomputing system. This system collectively has 323,872 CPU cores consisting of Skylake, Broadwell, Haswell, Ivy Bridge, and Sandy Bridge nodes. Skylake nodes, which consist of 40 cores and 192 GB of memory, are used for all CFD simulations in this paper. Data is saved to a 29 PB Lustre filesystem for solution post processing and animation.

4.1 Two-Dimensional Dynamic Stall

Dynamic stall is a challenging flow regime to accurately predict because an airfoil's large incidence results in flow separation and hysteresis of the forces and moments. Spatial and temporal algorithm accuracy, grid resolution and the turbulence model have a strong influence on the physical realism and accuracy of the computed flow. This two-dimensional problem is used to more readily study how the forces and moments converge in space and time using OVERFLOW's NB-AMR algorithm. This will provide guidance on how to apply this approach to the three-dimensional dynamic stall rotor problem.

Figure 9 shows the O-mesh grid topology for a NACA 0012 airfoil used for this study, which consists of 371x79 points in the circumferential and normal directions, respectively. There are 36 grid cells along the blunt trailing edge. The O-mesh is split into two grids with a total of 8 cells of overlap at each end because OVERFLOW's NB-AMR algorithm does not currently permit periodic boundary conditions. The far-field boundary is approximately 45 chord lengths away from the airfoil surface.

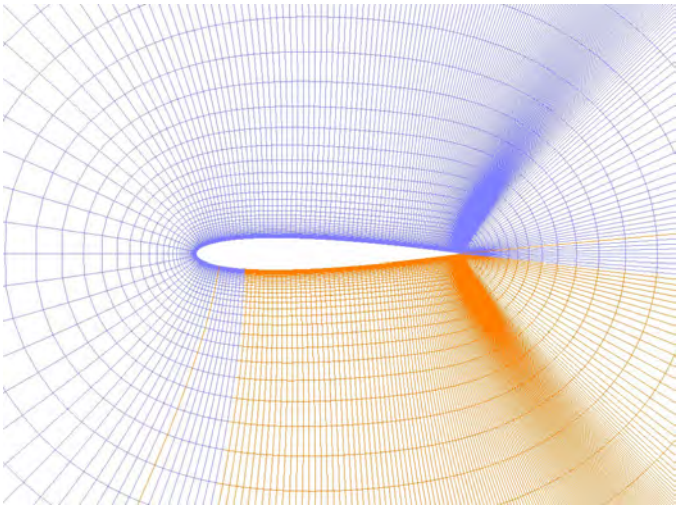

Figure 9 O-mesh for a NACA 0012 airfoil.

The angle of attack as a function of time is defined by

$$\alpha = 10° + 10° \sin\left(2kt - \frac{\pi}{2}\right) \tag{11}$$

where t is the non-dimensional time, $k = {}^{\omega c}/_{2U_\infty}$ the reduced frequency, ω the circular frequency, c the chord length, and U_∞ the freestream speed. Note that $0° \leq \alpha \leq 20°$. The solution process begins with a converged steady-state solution at α=0°, i.e., when t=0 and the airfoil is momentarily at rest. This initial condition is followed by 10 periods of oscillation to reach a converged periodic state.

The following NB-AMR nomenclature is used through this paper. NB-AMR0 refers to NB-AMR=0, i.e., a baseline case where there is no NB refinement; NB-AMR1 refers to NB-AMR=1, i.e., 1-level of near-body refinement; NB-AMR2 refers to NB-AMR=2, i.e., 2-levels of near-body refinement, etc.

Figure10 shows vorticity contours at selected angles of attack, and plots of the lift, drag, and pitching moment coefficients. The forces and moments are colored to indicate the upstroke and downstroke of the motion along with directional arrows. During a pitch cycle, a vortex forms near the leading edge and eventually advects downwind past the trailing edge. Lift stall, indicated by a sudden loss of lift, is associated with the vortex leaving the leading-edge region. Moment stall, indicated by a sudden negative nose-down pitching moment, is associated with the vortex passing over the trailing edge. Flow separation at the trailing edge is a third measure of the dynamic stall process. The forces and moments indicate a significant hysteresis with three stall events per cycle, which are slightly out of phase with each other. Each stall event is weaker than the previous one during the pitch cycle.

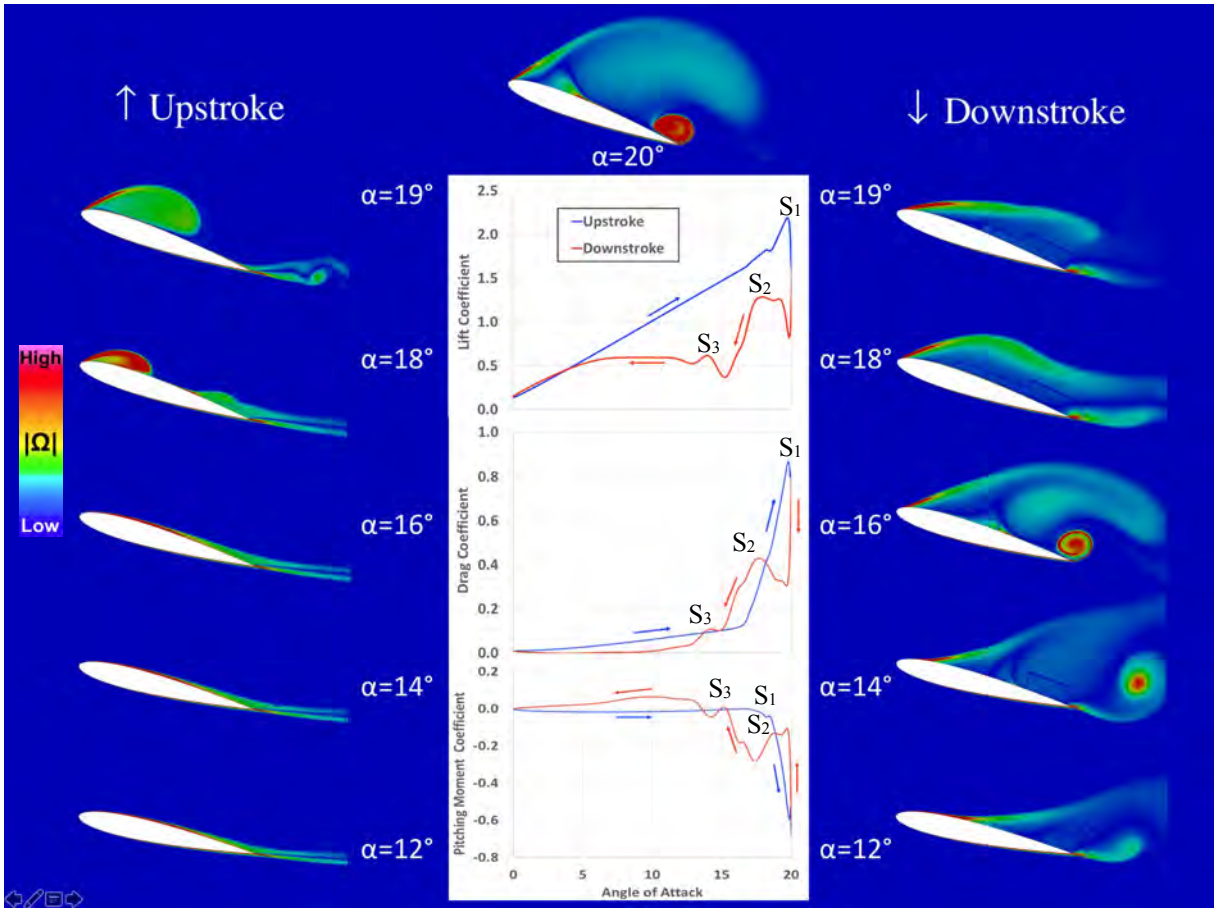

Figure 10 Visualization of vorticity contours, and plots of lift, drag and pitching moment coefficients with angle of attack. Three stall events, i.e., S_1, S_2 and S_3 are shown in the figure.

Figure 11 shows flow streamlines and the three-level near-body AMR grids (NB-AMR3) at α=20°. The streamlines are a realistic representation of the flow topology since the airfoil is momentarily at rest

at the apex of the pitching motion. These streamlines indicate a large primary leading-edge vortex, a small trailing edge vortex, and two secondary vortices near the airfoil leading edge. As the leading-edge vortex approaches the airfoil trailing edge, it induces an upwind velocity directly above the trailing-edge shear layer, while the flow below the shear layer has a downwind direction. These directionally opposing upper and lower velocities cause a shear-layer instability that rolls the shear layer up into a trailing-edge vortex. Although the nose-down pitching moment is associated with the leading-edge vortex passing over the trailing edge, it's the trailing-edge vortex that provides the local suction and nose down moment.

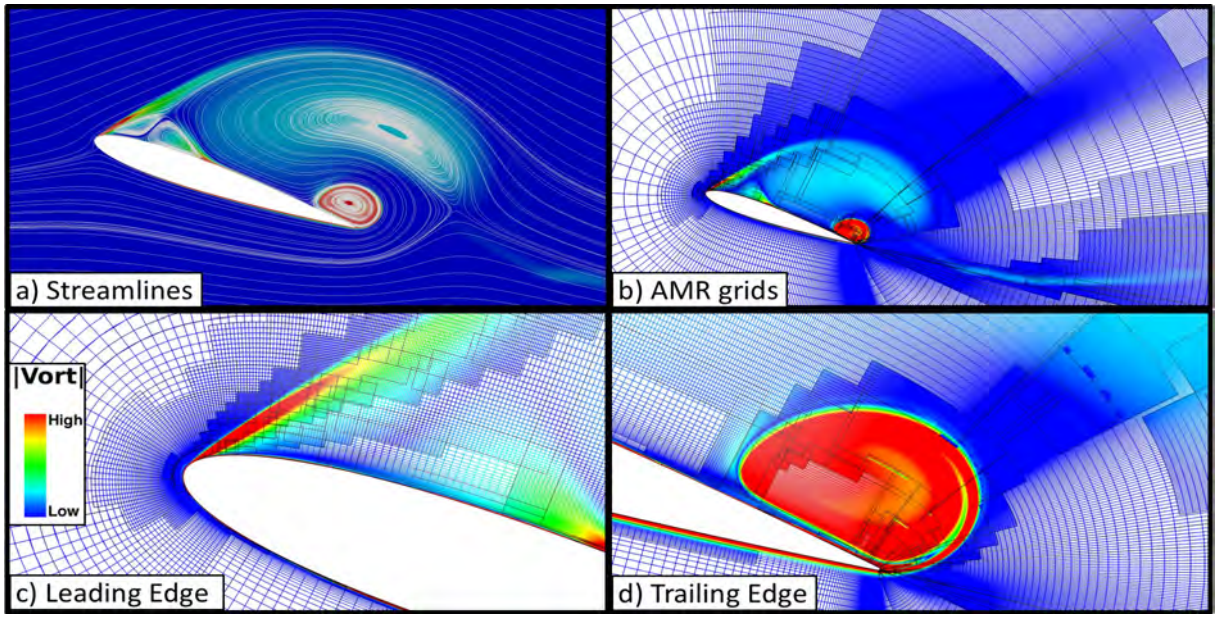

Figure 11 Dynamic stall streamlines and three levels of NB-AMR for a NACA 0012 airfoil at α=20°.

Figure 11 also shows the NB-AMR3 grids resolve the flow around the airfoil. The leading and trailing-edge vortices are automatically resolved to three levels, i.e., an 8X finer mesh in both coordinate directions. Additional resolution also occurs near the leading and trailing edges, where there are large flow gradients. The undivided difference sensing function, Eq. 3, captured these features well without the need to adjust the default AMR parameters. It was originally designed to require minimal attention.

Time convergence of the forces and moments with NB-AMR is now examined. Figure 12 shows how the RMS forces and moments change with the number of sub-iterations and near-body refinement. A comparison of RMS values takes into account the entire wave form, including all resolvable frequencies. This is a much stronger convergence criterion than using the mean. Each sub-iteration data point plotted in Fig. 12 was started from the previous one and run for two periods. The second period was found to be converged since the initial condition was sufficiently close. This approach allowed for more than 50 cases to be examined in an efficient manner. A green circle in the figure indicates that all differences in forces and moments are bounded by 0.25%, which is considered converged in this paper.

Figure 12 shows that the number of sub-iterations required for temporal convergence of the forces and moments increases with near-body refinement. This behavior is expected because the isotropic refinement results in finer meshes near the airfoil surface, especially in the body-normal direction. The situation can be further exacerbated by turbulent flow separation, which can lead to a stiff set of discrete equations and Courant-Friedrichs-Levy (CFL) restrictions. Initially the solution process converges in a smooth and nearly monotone manner but becomes more oscillatory and non-monotone with higher levels

of refinement. This required significantly more sub-iterations to ensure the converged result was bounded.

Figure 13, which is based on the converged green circled results of in Fig 12, shows how the drop in the L_2-norm dual-time residual varies with near-body refinement. It's interesting to note that as the grids are refined, the residual drop required for time accuracy decreases. It's not clear that this trend will continue. It's common practice with the OVERFLOW code to require a 2-order drop in the residual. These results indicate that the more difficult dynamic stall case should have at least a 2.5-order residual drop to ensure time accuracy.

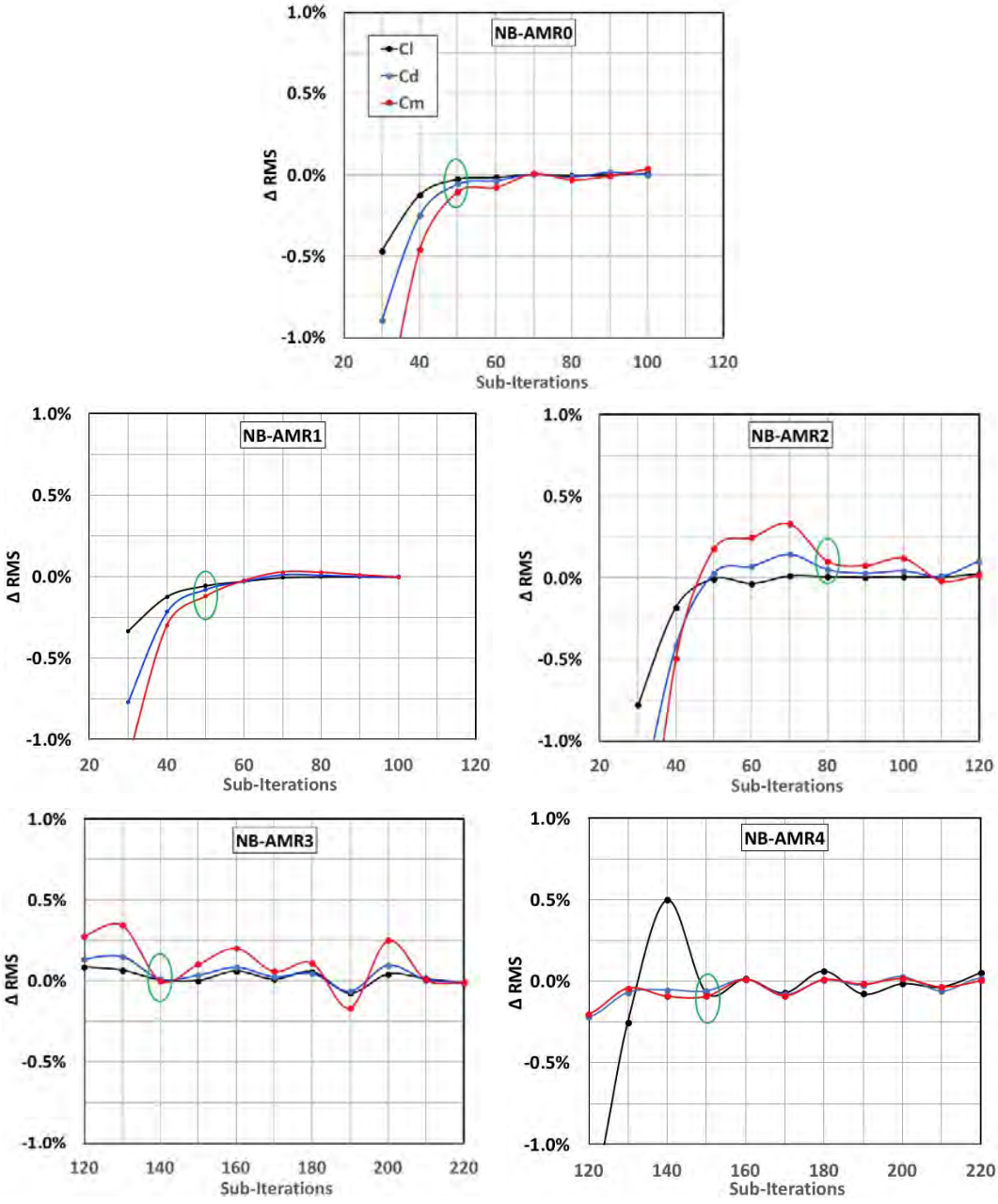

Figure 12 Second-order time-accuracy convergence. Percent change in the RMS lift, drag and pitching moment coefficients with sub-iterations. Green circle indicates change is bounded by 0.25%.

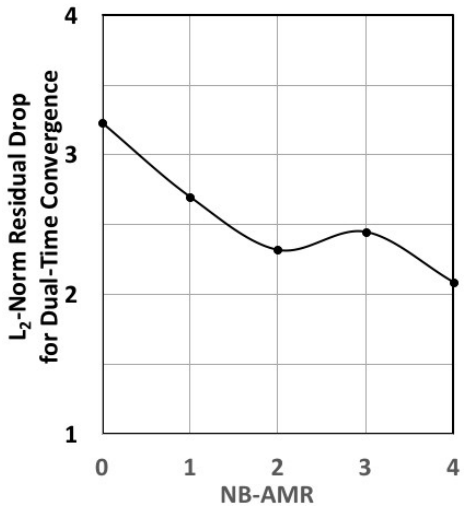

Figure 13 Required sub-iteration drop for temporal convergence. (See green circles in Fig. 12.)

The spatial convergence of the forces and moments with NB-AMR is now examined. Figure 14a compares the percent change in the RMS forces and moments with NB-AMR. For example, the result plotted at NB-AMR=2 compares the waveforms of levels 2 to 1, and so on. The change in RMS forces and moments are less than 1% for NB-AMR≥3 and considered sufficiently converged. Figure 14b shows that the RMS values of the forces and moments are relatively flat after 2 to 3 near-body refinements. The lift coefficient converges first, followed by the drag and pitching moment coefficients.

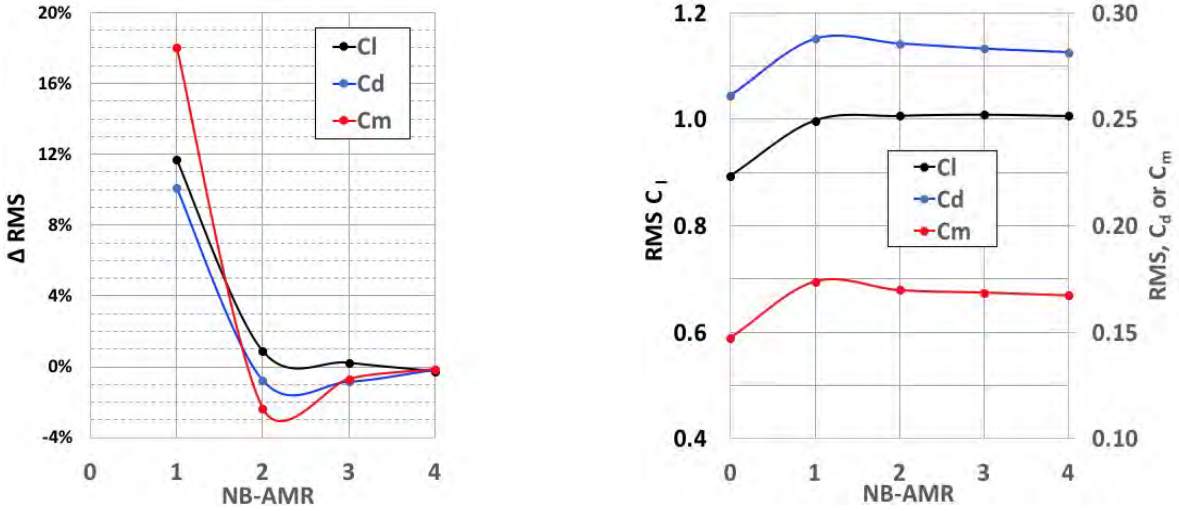

a) Percent change from previous NB refinement. **b)** RMS value.

Figure 14 Spatial convergence of lift, drag and pitching moment coefficients with NB-AMR.

Figure 15 shows the grid growth for the NACA 0012 airfoil with NB-AMR. Each level of grid refinement is reflected by a local increase in grid size by 4X. The three-dimensional problem will exhibit a more rapid 8X grid growth. So a reasonable baseline grid should be design to limit the number of AMR levels to two or three, when possible. This will also help mitigate the CFL restriction due to isotropic refinement.

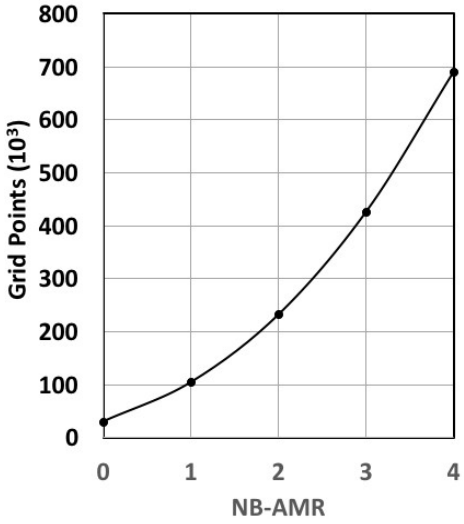

Figure 15 Grid growth with NB-AMR.

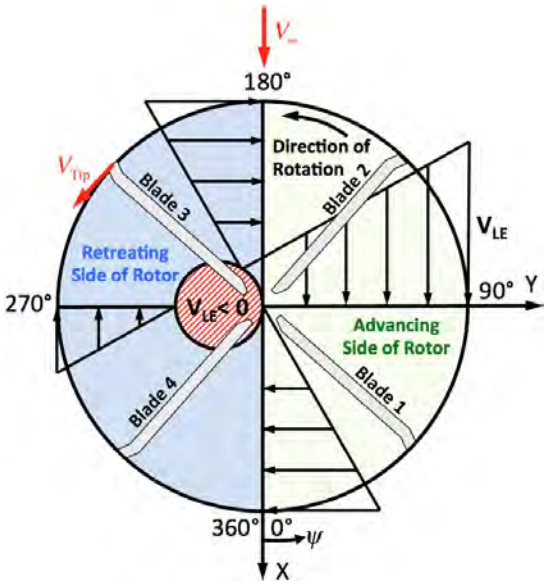

Figure 16 Flow conditions for forward flight.

4.2 Three-Dimensional Dynamic Stall

Dynamic stall usually occurs when helicopters operate at high flight speeds or during high load-factor maneuvers. This occurs because the generated thrust must keep the vehicle aloft while providing the propulsive force for forward flight. By contrast, fixed-wing aircraft usually experience stall at low flight speeds.

Figure 16 represents the flow conditions experienced by a UH-60A rotor in forward flight. Initially, blade 1 of the rotor is aligned with the x axis (ψ=0 deg). This represents the starting point of an impulsive start CFD solution, and an azimuthal reference point. The x-axis also represents the nominal direction of the freestream velocity, V_∞. The rotor blade advances into the headwind on the right side of the diagram while it retreats away from the headwind on the left side of the diagram.

The incident velocity normal to the blade's leading edge is also shown in the figure for azimuth angles of ψ=0, 90, 180, and 270 deg. This local leading-edge velocity, V_{LE}, is the sum of the rotor rotational speed and the normal component of the vehicle flight speed. The rotor blades experience a region of reversed flow, shown by a red circle, where the flow is directed from the local airfoil trailing edge towards the leading edge. The advance ratio, $\mu=V_\infty/V_{tip}$, is the normalized diameter of this circle. As the rotor blade advances into the headwind it usually operates at a lower angle of attack, providing sufficient lift while avoiding strong shocks and flow separation. As the rotor blade retreats away from the headwind it experiences a lower relative velocity, requiring the blade to pitch up to higher angles of attack.

Flight counter C9017 is a flow condition where the UH-60A rotor experiences dynamic stall. Figure 6 shows a side view of the OB-AMR grids automatically capturing the rotor wake, which is visualized by gray-scale vorticity contours. This rotor wake is resolved using ΔS=5% c_{tip}, and consists of approximately 3,700 grids and 210 million grid points. Reference [6] showed that finer wake-grid resolutions did not affect the predicted airloads. This baseline grid resolution, whose body grid size is summarized in Table 3, represents a best attempt to predict the airloads without the use of NB-AMR.

Figure 17 shows an oblique view of the rotor's tip vortices and wake. Note that the nature of this flow is much more complex than the 2D airfoil example shown in Fig. 10. The flow is relatively attached on the advancing side and separated on the retreating side.

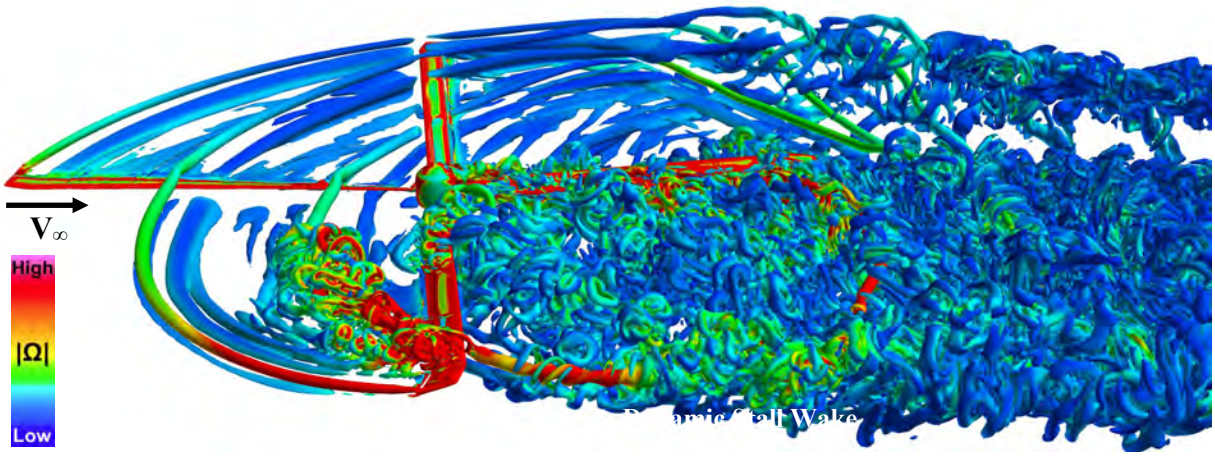

Figure 17 Oblique view of vortex wake (q-criterion iso-surfaces) colored by vorticity magnitude.. Baseline resolution: no NB-AMR, OB-AMR spacing ΔS=5% c_{tip}, and approximately 3,700 grids and 210 million grid points.

Figure 18 illustrates some of the marked differences between 2D and 3D dynamic stall. The two frames in the figure show Blade 1 at two separate times. The first frame, ψ=180°, shows the vortices of Blades 2 and 3 passing over Blade 1 with no local flow separation. The second frame, ψ=225°, shows outboard and inboard flow separation on Blade 1, due to the vortices from Blades 2 and 3. This BVI induced dynamic stall was first observed in Ref [6]. The swirl of a vortex causes a local increase in angle-of-attack along the outboard side of the vortex and a decreased angle-of-attack along the inboard side of the vortex. In this case, the flow separates outboard of the two vortices and remains attached inboard of the two vortices. When Blade 1 rotates through the 3rd-quadrant, the Blade 2 vortex moves towards the Blade 1 tip and the Blade 3 vortex moves towards the Blade 1 root. A time-dependent animation of this flow shows each separation moving along the Blade 1 span with these vortices, and a region of attached flow in between, see Fig. 18. Chaderjian [6] also showed a good correlation of the CFD vortex positions on Blade 1 and the locations of the two dynamic stall events reported by Bousman's analysis of the flight-test data [1].

Figure 18 shows two other differences between 2D and 3D dynamic stall. 2D dynamic stall involves a leading-edge vortex that lifts off from the airfoil leading edge and advects downwind, past the airfoil trailing edge, see Fig. 10. Something similar happens in 3D, however, Helmholtz's vortex theorem states that a vortex line can not terminate within a fluid, but on a boundary. Thus, when the 3D leading-edge vortex begins to lift off the rotor blade, the vortex line must close in on itself and form a vortex ring. Figure 18 shows that several vortex rings are emitted as the stall progresses along the blade span during blade rotation. Figure 18 (ψ=225°) also shows that the path of the Blade 2 vortex changes due to flow separation on Blade 1. This can alter the airloads and BVI noise on the following blade.

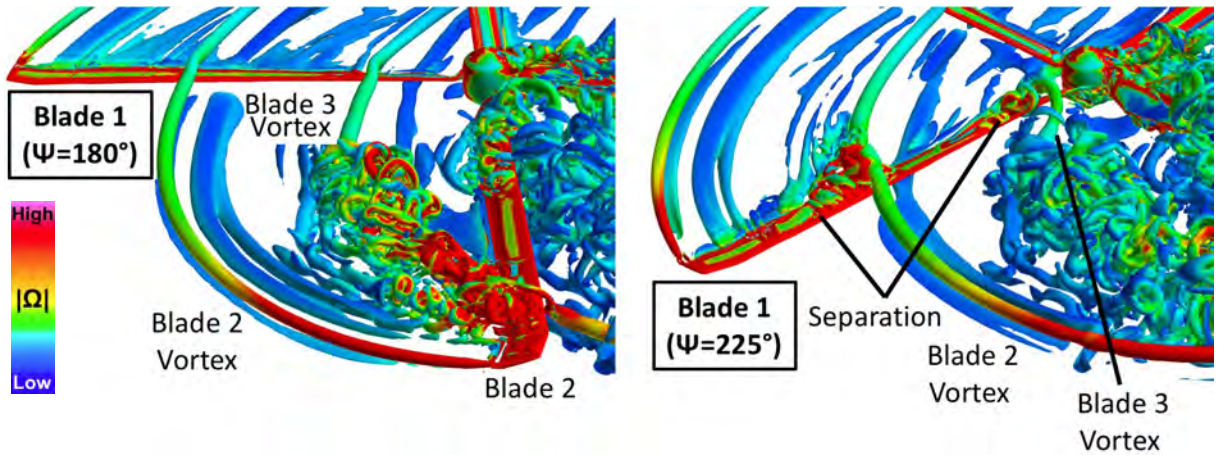

Figure 18 Close-up view of blades one and two. $\Delta\psi_{Blade\ 1}$=45°, NB-AMR0, ΔS=5% c_{tip}.

Figure 19 shows the loose coupling convergence history for the baseline resolution pitch, flap, and lag control angles, along with their first harmonics. These motions are applied at the blade root, see Eq. 8. All the control angles are converged within 5 revolutions from impulsive start and run further to 10 revolutions. The pitch and lag angles do have some small oscillations. This is caused by a small aperiodicity on the blade airloads due to turbulent flow separation.

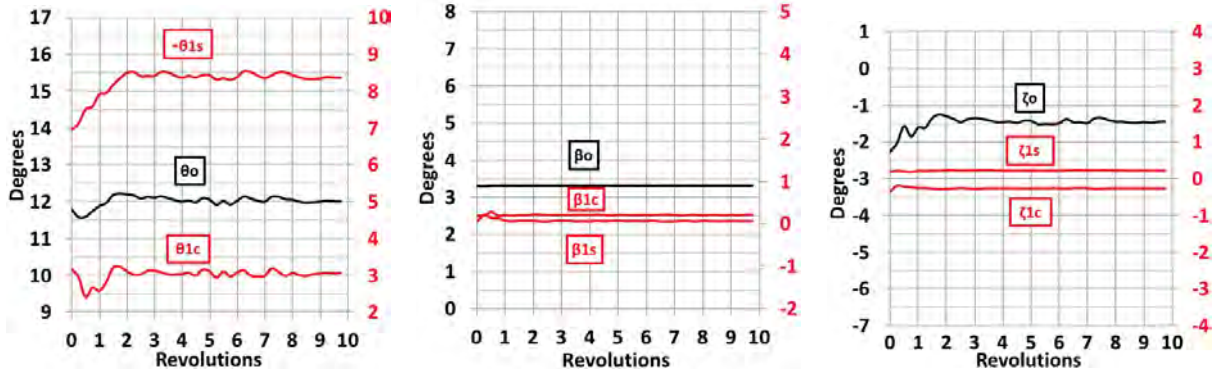

Figure 19 Loose coupling convergence history for the baseline resolution pitch, flap, and lag control angles.

Near-body AMR was also applied to the UH-60A rotor grid system. The aeroelastic deflections (and control angles) were "frozen" at 10 revolutions to allow for a more direct comparison of the near-body refinement solutions. Each near-body refinement solution was started from a previous result and run for two additional rotor revolutions, i.e., AMR1 begins from the converged AMR0 solution and AMR2 begins from the converged AMR1 solution. The forces and moments were found to be converged on the second period. Based on the previous 2D time-accuracy study, all UH-60A solutions had at least a 2.5-order L_2-norm drop in the dual-time residual. Table 5 summarizes the time step and number of sub-iterations used to maintain time accuracy. The time step was reduced for the NB-AMR cases to keep the number of sub-iterations near 100.

Near-body refinement was turned off within a distance of 2% c_{tip} of the blade surface. This was done for two reasons. First, NB-AMR resulted in very fine meshes and low y^+ values near the blade surface. It was difficult to maintain code stability due to CFL restrictions. The baseline mesh was already very fine, well within $y^+<1$ over most of the blade surface. Secondly, each curvilinear body grid had 100 grid cells

in the normal direction, with about 60 grid cells within the attached boundary layers. Applying NB-AMR down to the blade surface over resolved the boundary layer, resulting in rapid grid growth to over 1 billion grid points for NB-AMR2. Both of these negative attributes are expected when using isotropic NB-AMR.

Table 5 Summary of NB-AMR 2nd-order time accuracy parameters.

Near-Body Refinement	Time Step (revs)	Sub-iterations
NB-AMR0	1/4°	100
NB-AMR1	1/8°	90
NB-AMR2	1/8°	130

Figure 20 compares the computed and measured normal force coefficient (mean removed) at four radial locations, see Fig. 3, for NB-AMR0, NB-AMR1 and NB-AMR2. There is overall good agreement between computation and experiment, however, the drop in normal force is under predicted near ψ=90° for the outboard sections. This is surprising because the flow is attached and relatively benign in that region. On the other hand, the comparisons are better at the first stall event (220°≤ψ≤270°) and the second stall event (330°≤ψ≤360°). Refining the blade meshes with up to two-levels of NB-AMR has little effect. There is similar agreement between the computed pitching moment coefficient (mean removed) and the flight-test data, see Fig. 21.

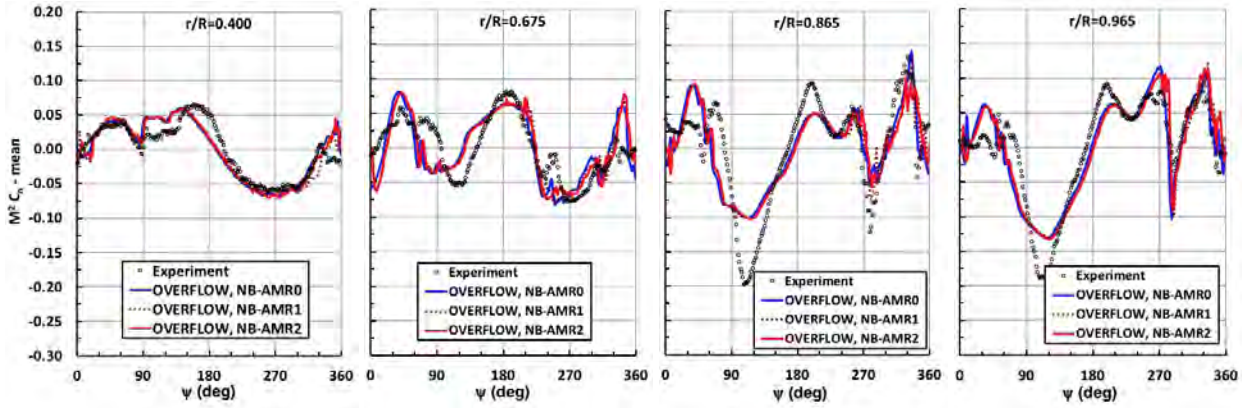

Figure 20 Comparison of normal force coefficient (mean removed) at four radial stations.

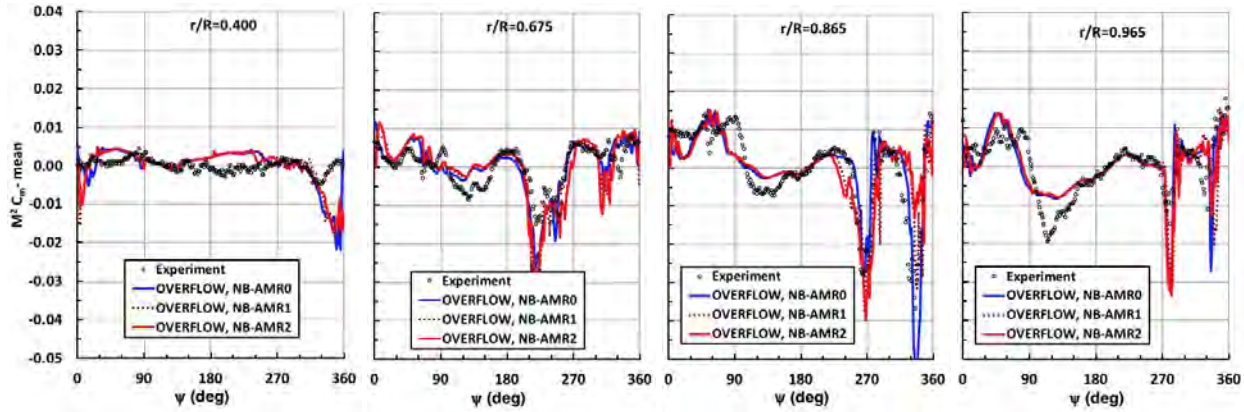

Figure 21 Comparison of pitching moment coefficient (mean removed) at four radial stations.

These two figures indicate that the CFD solutions are grid converged. It is unlikely that the turbulence model is responsible for the noted discrepancies at ψ=90° since the solution compared better with flight-test data on the retreating side, where stall occurs, than on the advancing side, where the flow is mostly attached. It is more likely that uncertainties in the rotor blade aeroelastic properties, such as moments of inertia, or flight-test measurement discrepancies reported in Ref [11] are responsible for these differences.

Figure 22 displays four frames taken from a time-dependent animation showing the dynamic nature of the NB-AMR2 process. An outline of the near-body grids are shown on selected spanwise stations and colored by a transparent vorticity magnitude. The transparency highlights flow structures near the blade surface while deemphasizing flow structures away from the blade surface. These images show fewer AMR grids on the advancing side, ψ=90° and 180°, where the flow is relatively attached, and more AMR grids on the retreating side, ψ=270° and 360°, where the flow is separated. The NB-AMR process is refining the flow physics where it is needed, and with greater efficiency than using uniform grid refinement throughout the entire NB grids.

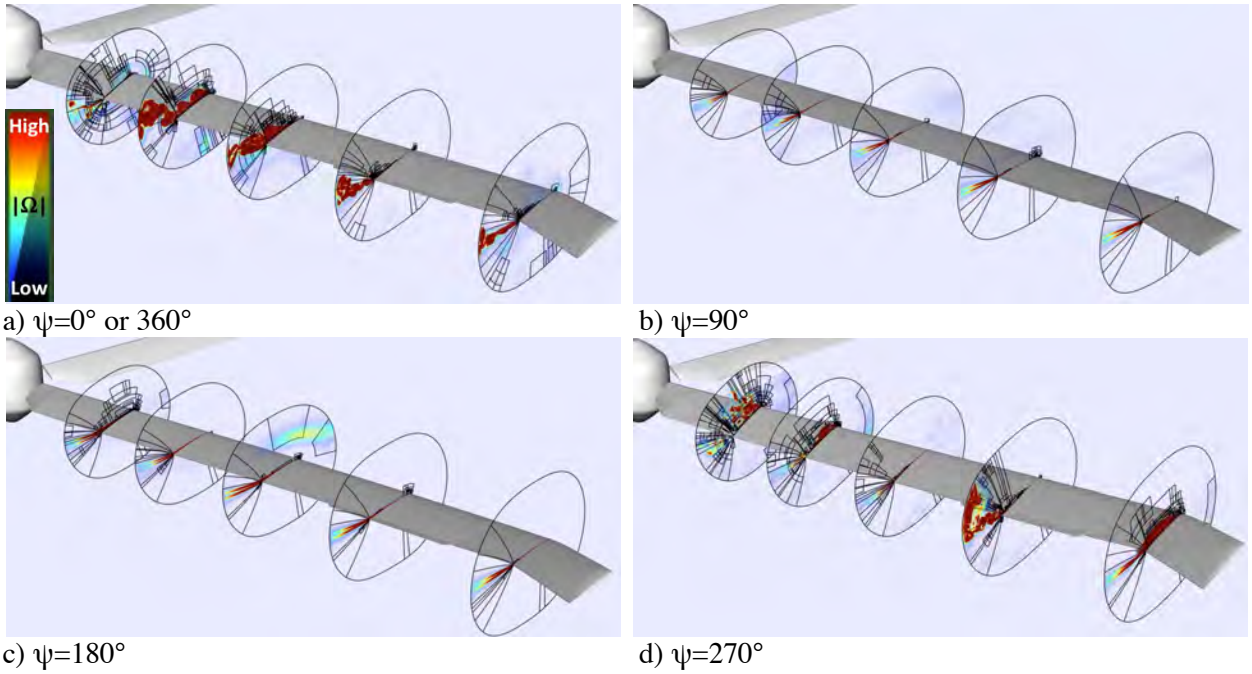

a) ψ=0° or 360° b) ψ=90°

c) ψ=180° d) ψ=270°

Figure 22 Outline of NB-AMR2 grids at selected spanwise locations on a rotor blade.

Figure 23 provides a closeup view of the third quadrant vortex wake for NB-AMR0, NB-AMR1 and NB-AMR2. The NB-AMR1 and NB-AMR2 solutions provide greater detail of the flow separation and vortex rings than the baseline NB-AMR0 case. However, it is also noted that the flow structures for NB-AMR1 and NB-AMR2 are almost indistinguishable. This supports the conclusion, together with Figs. 20-21, that the flow is both quantitatively and qualitatively grid resolved.

Figure 24 shows two snapshots in time from animations of the NB-AMR0 and NB-AMR2 simulations. These correspond to the first stall event at ψ=270°. The viewpoint moves with the blade tip and shows transparent vorticity magnitude contours along the blade's span. Similar to Fig 23, NB-AMR2 provides greater detail of the dynamic stall flow separation than NB-AMR0.

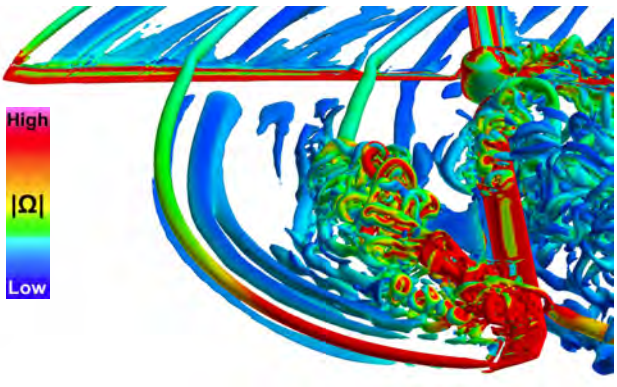

a) NB-AMR0

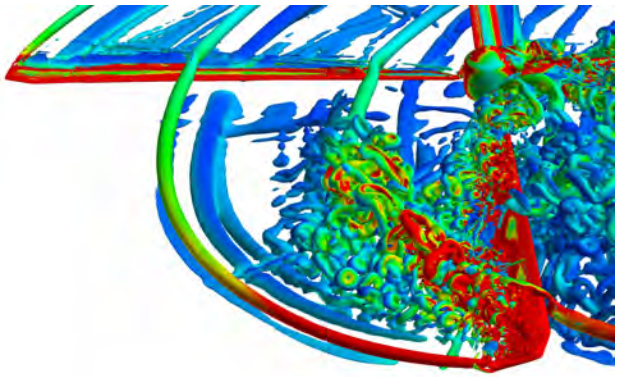

b) NB-AMR1

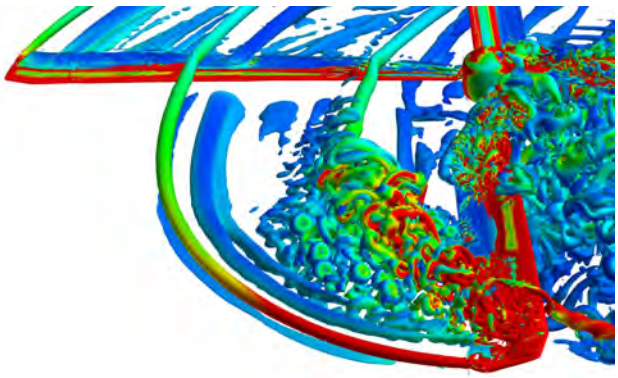

c) NB-AMR2

Figure 23 Close up view of vortex wake at ψ=270°. Q-criterion colored by vorticity magnitude.. .

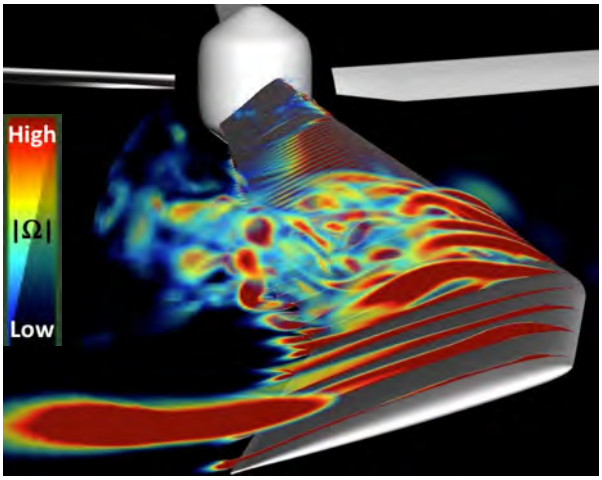

b) NB-AMR0

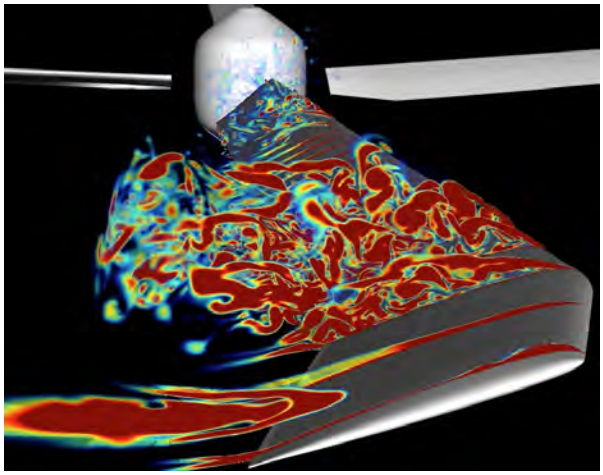

b) NB-AMR2

Figure 24 Snapshot from time-dependent animation (ψ=270°). Cutting planes colored by transparent vorticity magnitude.

Table 6 summarizes the computer wall-clock time used for the three NB-AMR resolutions. The computer time and cost grow significantly with NB-AMR grid refinement (see 4th column). However, the computational efficiency (see 6th column) also degrades significantly. On the other hand, the

computational efficiency was found to improve with OB-AMR grid refinement, see Table 7 from Ref [6]. These opposite trends are probably attributed to at least two factors: 1) The computational cost/grid point is higher for curvilinear grids than Cartesian grids; 2) NB-AMR has slower temporal convergence than OB-AMR due to CFL restrictions. This second issue is related to isotropic grid refinement on highly non-isotropic body grids, especially with fine grid spacing normal to the viscous wall.

Table 6 Summary of computer wall-clock time using 5,600 Skylake CPU cores with two threads.

Flight Counter C9017 - (Dynamic Stall)					
NB-AMR Resolution	# Grids	# Grid Points	Time/Rev	Relative Time	Time/Rev/ 100 Million GP
NB-AMR0	3,700	210 million	6.6 hr	1.0	3.1
NB-AMR1	8,000	360 million	17.6 hr	2.7	4.9
NB-AMR2	14,533	675 million	60.4 hr	9.2	8.9

Table 7. Summary of computer wall-clock time using 5,600 Broadwell CPU cores with two threads [6].

Flight Counter 9017 – (Dynamic Stall)					
OB-AMR Resolution	# Grids	# Grid Points	Time/Rev	Relative Time	Time/Rev/ 100 Million GP
$\Delta S=10\%c_{tip}$	870	78 million	5.6 hr	1.0	7.2
$\Delta S=5\%c_{tip}$	3,200	236 million	9.5 hr	1.7	4.0
$\Delta S=2.5\%c_{tip}$	14,500	1.29 billion	26.0 hr	4.6	2.0

5. Conclusions

Time-dependent flow simulations for a NACA 0012 airfoil and a flexible UH-60A Blackhawk helicopter rotor undergoing dynamic stall has been carried out using the OVERFLOW Navier-Stokes CFD code. Second-order dual-time accuracy and 5th-order spatial accuracy was used throughout this study. OVERFLOW's NB-AMR was used to improve the curvilinear body-grid resolution while OB-AMR was used to resolve the UH-60A rotor wake with a Cartesian grid spacing of $\Delta S=5\%c_{tip}$. The Spalart-Allmaras RANS turbulence model was used for 2D flows while the hybrid RANS/LES model (DDES) was used for 3D flows.

NACA 0012 Airfoil Results

Up to four levels of NB-AMR where applied to a baseline O-mesh.

- The 2nd-order undivided difference sensing function performed well, automatically finding all relevant flow features. There was no need to change the default sensor parameters, making it easy to use.
- The number of dual-time sub-iterations increased from 50-150 with NB refinement. This bounded the change in RMS lift, drag and pitching moment coefficients within 0.25%.
- A 2.5-order L_2-norm sub-iteration drop is recommended to maintain 2nd-order dual-time accuracy for dynamic stall.
- The change in RMS lift and drag coefficients were bounded within 1% with two levels of NB refinement while the pitching moment coefficient required three levels of refinement.
- Isotropic grid refinement produced rapid grid growth. A baseline grid should be designed so that only 2-3 levels of NB-AMR are needed to achieve a grid-converged solution.

UH-60A Rotor Results

- 3D dynamic stall was significantly more complex and different than 2D dynamic stall. Some of these differences include:
  - BVI-induced flow separation.
  - The release of vortex rings from the rotor blades rather than simple 2D vortices.
  - Flow separation can alter the path of blade-tip vortices, possibly affecting the following blade's airloads and acoustics.
- NB-AMR was considerably more difficult to apply in three dimensions. It was turned off within 2% c_{tip} of the rotor blade surface, typically well within the blade's boundary layer.
  - It was difficult to maintain algorithm stability when applying NB-AMR all the way to the blade surface, mostly due to CFL stability restrictions.
  - Turning off NB-AMR near the blade surface also helped control grid growth, especially in separated flow regions. Two levels of unrestricted NB-AMR resulted in over 1 billion grid points.
- There was little change in the blade sectional airloads, even with two levels of NB-AMR.
  - The baseline solution is grid converged.
  - There was overall good agreement between CFD and flight-test measured airloads.
  - The agreement was better on the retreating side, where there is dynamic stall and significant flow separation, compared to the advancing side, which is mostly attached flow. It is more likely that these differences are due to uncertainties in the aeroelastic blade properties or flight-test measurements rather than the turbulence model.
- Time-dependent flow animations provided insight into the NB-AMR process.
  - NB-AMR provided much finer resolution and detail of the separated flow.
  - The 2nd-undivided difference sensor function performed well, finding all relevant flow features without any user adjustment, similar to the 2D results.
- Computational efficiency was found to improve with OB-AMR but decrease with NB-AMR.
  - There are at least two reasons for this difference.
    - The computational cost/grid point is higher for curvilinear grids than Cartesian grids
    - NB-AMR has slower temporal convergence than OB-AMR due to CFL restrictions.
- A non-isotropic NB-AMR process would probably alleviate some of these NB refinement difficulties.

Acknowledgements

The author would like to thank NASA's Revolutionary Vertical Lift Technology Project (RVLT) for supporting this work. The author would also like to thank Mr. Timothy Sandstrom of NASA's Advanced Supercomputing (NAS) Data Analysis & Visualization Group for his time-dependent flow animations.

References

[1] Bousman, W. G., "A Qualitative Examination of Dynamic Stall from Flight Test Data," *Journal of the American Helicopter Society*, Vol. 43, (4), Oct. 1998, pp. 279-295.

[2] Nichols, R., Tramel, R., and Buning, P., "Solver and Turbulence Model Upgrades to OVERFLOW 2 for Unsteady and High-Speed Flow Applications," AIAA-2006-2824, June 2006.

[3] Nichols, R., and Buning, P., "User's Manual for OVERFLOW 2.1," University of Alabama at Birmingham, Birmingham, AL, 2008.

[4] Chaderjian, N. M., and Buning, P. G., "High Resolution Navier-Stokes Simulation of Rotor Wakes," Proceedings of the American Helicopter Society 67th Annual Forum, Virginia Beach, VA, May 3-5, 2011.

[5] Chaderjian, N. M., "Advances in Rotor Performance and Turbulent Wake Simulation using DES and Adaptive Mesh Refinement," Paper Number ICCFD7-3506, Presented at the 7th International Conference on Computational Fluid Dynamics (ICCFD7) on the Big Island of Hawaii, July 9-13, 2012.

[6] Chaderjian, N. M., "Navier-Stokes Simulation of UH-60A Rotor/Wake Interaction Using Adaptive Mesh Refinement," Presented at the American Helicopter Society 73rd Annual Forum, Fort Worth, TX, May 9-11, 2017.

[7] Lim, J. W., Nygaard, T. A., Strawn, R., and Potsdam, M, "Blade-Vortex Interaction Airloads Prediction Using Coupled Computational Fluid and Structural Dynamics," *Journal of the American Helicopter Society*, Vol. 52, (4), Oct. 2007, pp. 318-328.

[8] Jia, Z., Lee, S., and Brentner, K. S., "Assessment of Turbulence Modeling and Wake-Grid Resolution for Lift-Offset Coaxial Rotor Simulations," to be presented at the AIAA Applied Aerodynamics Conference, Atlanta, GA, June 25-29, 2018

[9] Biedron, R. T., and Lee-Rausch, E. M., "An Examination of Unsteady Airloads on a UH-60A Rotor: Computation versus Measurement," Presented at the American Helicopter Society 68th Annual Forum, Fort Worth, TX, May 1-3, 2012.

[10] Bousman, W. G., and Kufeld, R. M., "UH-60A Airloads Catalog," NASA TM 2005-212827, Aug. 2005.

[11] Potsdam, M., Yeo, H., and Johnson, W., "Rotor Airloads Prediction Using Loose Aerodynamic/Structural Coupling," *Journal of Aircraft*, Vol. 43, No. 3, May-June 2006, pp. 732-742.

[12] Pulliam, T. H., and Chaussee, D. S., "A Diagonal Form of an Implicit Approximate-Factorization Algorithm," *Journal of Computational Physics*, Vol. 39, No. 2, 1981, pp. 347-363.

[13] Pulliam, T. H., "High Order Accurate Finite-Difference Methods: as seen in OVERFLOW," AIAA-2011-3851, June 2011.

[14] Buning, P. G., and Pulliam, T. H., "Cartesian Off-Body Grid Adaption for Viscous Time-Accurate Flow Simulations," AIAA-2011-3693, June 2011.

[15] Buning, P. G., and Pulliam, T. H., "Near-Body Grid Adaption for Overset Grids," AIAA-2016-3326, June 2016.

[16] Spalart, P. R., and Allmaras, S. R., "A One-Equation Turbulence Model for Aerodynamic Flows," AIAA-92-0439, January 1992.

[17] Ramasamy, M., Johnson, B., and Leishman, J. G., "Turbulent Tip Vortex Measurements Using Dual-Plane Digital Particle Image Velocimetry," Proceedings of the American Helicopter Society 64th Annual Forum, Montréal, Canada, April 29-May 1, 2008.

[18] Shur, M. L., Strelets, M. K., Travin, A. K., and Spalart, P. R., "Turbulence Modeling in Rotating and Curved Channels: Assessing the Spalart-Shur Correction," *AIAA Journal,* Vol. 38, No. 5, May 2000, pp. 784-792.

[19] Smagorinsky, J., "General Circulation Experiments with the Primitive Equations. I. The Basic Experiment," *Monthly Weather Review*, Vol. 91, No. 3, pp. 99-164.

[20] Spalart, P., Jou, W-H., Strelets, M., and Allmaras, S. "Comments on the Feasibility of LES for Wings and on a Hybrid RANS/LES Approach," First AFOSR Conference on DNS/LES, August 1997, Greyden Press, Columbus, OH.
[21] Spalart, P. R., Deck, S., Sur, M. L., Squires, K. D., Strelets, M., and Travin, A., "A New Version of Detached-Eddy Simulation, Resistant to Ambiguous Grid Densities," *Theoretical and Computational Fluid Dynamics (2006)*, Vol. 20, No. 3, pp. 181-195.
[22] Johnson, W., "Rotorcraft Aerodynamic Models for a Comprehensive Analysis," American Helicopter Society 54th Annual Forum, Washington, D.C., May 1998.